Investigation of the microstructure and mechanical properties of high pressure die casting AE81 magnesium alloy automotive components

Hecong Xie^{1,2}, Jiangfeng Song^{1,2,*}, Chuangming Li^{1,2}, Zhihua Dong^{1,2}, Ang Zhang^{1,2}, Jiang Zheng^{1,2}, Daoyan Yang³, Wei Ren³, Xianyue Qin³, Hongfen Feng⁴, Dongxia Xiang⁵, Bin Jiang^{1,2,**}

- 1. National Engineering Research Center for Magnesium Alloys, Chongqing University, Chongqing, 400044, China
- 2. National Key Laboratory of Advanced Casting Technologies, Chongqing University, Chongqing, 400044, China
 - 3. Chongqing Boao Mg-Al Manufacturing Co., Ltd, Chongqing 400800, China
 - 4. Shanxi Yinguang Huasheng Magnesium Industry Co., Ltd, Shanxi 043800, China
 - 5. Chongqing Advanced Light Metal Research Institute, Chongqing 400044, China

*Corresponding author at: National Engineering Research Center for Magnesium Alloys, Chongqing University, Chongqing, 400044, China. E-mail address: jiangfeng.song@cqu.edu.cn (J Song), jiangbinrong@cqu.edu.cn (B. Jiang).

Abstract:In this study, AE81 magnesium alloy castings for electric vehicle battery module end were fabricated using high pressure die casting (HPDC), and the effects of filling behavior and solidification sequence on the spatial distribution of microstructure and mechanical properties were systematically investigated. The results indicate that along the flow path toward the overflow gate, the area fraction of externally solidified crystals (ESCs) decreases gradually, and the average grain size becomes finer, resulting in a slight increase in yield strength. Conversely, the pores volume fraction significantly affects ductility and tensile strength, with the gate region exhibiting the highest porosity (0.74%) and thus the lowest elongation (4.3%) and ultimate tensile strength (218 MPa). In other regions, the porosity decreases to 0.33–0.39%, resulting in increased elongation (6–7%) and higher ultimate tensile strength (235–242 MPa). Analysis of the microstructure-property relationship reveals that the yield strength follows the Hall-Petch relationship, while elongation and tensile strength are negatively correlated with pore volume fraction. This finding elucidates the mechanism behind the formation of performance gradients in HPDC magnesium alloys and provides a theoretical basis for the design of lightweight components in new energy vehicles.

Keywords: High pressure die casting; AE81 magnesium alloy; Battery module end; Microstructure; Mechanical properties; Pore

1 Introduction

In response to the twin challenges of environmental deterioration and energy scarcity worldwide, the promotion of new energy vehicles has become a viable strategy for lowering CO2 emissions and reducing reliance on fossil fuels [1-4]. Against this backdrop, vehicle lightweighting technology has attracted considerable attention as a key direction for the development of electric vehicles. Magnesium alloys, owing to their low density (only two-thirds that of aluminum and one-quarter that of steel) [5, 6], high specific strength [7], and excellent damping capacity [8], are widely recognized as the most lightweight metallic materials. These promising characteristics endow magnesium alloys with significant engineering value in weight reduction for new energy vehicles [9, 10], especially in the lightweight design of key components such as battery pack structures and vehicle body frames.

High pressure die casting (HPDC) is a key manufacturing technique for magnesium alloy automotive parts, known for its superior surface quality and ability to fabricate thin-walled, intricate components [11, 12]. Compared with aluminum alloys, HPDC of magnesium alloys significantly extends die life and improves production efficiency. It has been widely applied in mass production of small to medium-sized structural components such as steering wheels, shock towers, and dashboard brackets, achieving notable energy-saving and emission-reduction benefits [3]. However, commercially used die-cast magnesium alloys are still mainly limited to low-strength AM series (AM50A, AM60B) [13, 14] and AZ series (AZ91D) [15], whose room-temperature mechanical properties are generally low, making them inadequate for structural applications in electric vehicles. To overcome AFC.

this technical bottleneck, our research team has developed a novel HPDC AE81 magnesium alloy (Mg–8Al–0.7Zn–1.5Ce–0.25Mn–0.25Sb–0.1Sr) through a multi-element microalloying design approach [16]. While maintaining cost competitiveness, this alloy exhibits an excellent combination of mechanical properties, with a room-temperature yield strength (YS) of 190 ± 6.1 MPa, an ultimate tensile strength (UTS) of up to 290 ± 9.8 MPa, and an elongation (EL) of approximately 10%, achieving an optimal balance of strength, ductility, and economy. It offers an ideal lightweight material solution for critical load-bearing components in electric vehicles.

During the HPDC process of automotive thin-walled structural components, the metal melt undergoes complex physical phenomena including slow movement in the shot sleeve, high-speed and high-pressure mold filling, and non-equilibrium solidification [17, 18]. These phenomena inevitably lead to heterogeneity in microstructure and mechanical properties. A study by Niu et al. [19] focused on the microstructural and mechanical characteristics of large-scale thin-walled HPDC aluminum alloy castings with a melt flow length of 1230 mm. Their results revealed that along the melt flow direction from the gate to the overflow, both the size and fraction of coarse α -Al grains decreased, accompanied by a reduction in average grain size, resulting in a slight increase in YS. With increasing melt flow distance, the pore volume fraction significantly increased, which in turn led to a sharp decline in alloy ductility. It has been reported that filling conditions, heat transfer behavior, solidification sequence, and cooling rate within the mold cavity significantly affect the microstructure and mechanical properties of HPDC castings [20-22]. Notably, there remains a significant gap in the literature concerning the correlation between microstructure and mechanical properties in complex thin-walled HPDC magnesium alloy components. In particular, the coupling mechanism between melt flow patterns and solidification sequence in controlling the spatial distribution of properties has yet to be elucidated. Addressing this scientific issue holds substantial engineering significance for achieving precise control over the performance of large, thin-walled magnesium alloy castings.

X-ray computed tomography (CT), as a non-destructive three-dimensional (3D) characterization method, has evolved into an essential analytical tool for investigating alloy solidification dynamics, spatial distribution of secondary phases, and the evolution of pore defects [23-27]. This technique enables precise quantification of dendritic morphology evolution, volume fraction and size distribution of secondary phases, and pore network connectivity, contributing to significant advances in materials science research [28-30]. It serves as an indispensable tool for uncovering the mechanisms underlying defect formation in HPDC magnesium alloys. In this study, AE81 magnesium alloy battery module end castings were successfully fabricated using the HPDC Α comprehensive investigation of microstructure and properties of HPDC AE81 magnesium alloy battery module ends was conducted using scanning electron microscopy (SEM), X-ray CT, and finite element modeling. Fundamental characteristics, including defect distribution, mechanical properties, microstructure, and fracture morphology at different casting locations, were evaluated. Finally, the study examined the microstructural heterogeneity induced by melt flow and casting solidification. This provides theoretical guidance for improving the tensile properties of HPDC AE81 magnesium alloy castings.

2 Experimental procedure

The preparation of the HPDC AE81 magnesium alloy battery module end in this work comprised metal melting, casting, and die casting steps. Prior to melting, high-purity Mg (99.9%), Zn (99.9 wt.%), Al (99.9 wt.%), Sb (99.9 wt.%), and master alloys including Mg-10 wt.% Mn, Mg-30 wt.% Sr, and Mg-30 wt.% Ce were used according to the designed composition ratio. Pure Mg was first heated in a resistance furnace. Upon reaching ~500 °C, a protective gas mixture of CO₂ and SF₆ (volume ratio 100:1) was introduced to prevent oxidation. Once the pure Mg was fully molten, the master alloys were gradually added, and the furnace temperature was raised to 740 °C. After complete melting, the alloy melt was refined for 5-10 minutes, followed by slag removal. The melt was allowed to cool naturally to 720 °C and held for approximately 15 minutes before casting. Subsequently, the prepared AE81 melt was poured into a 650-ton cold-chamber die casting machine (YIZUMI D-M650) to produce the castings shown in Fig. 1(a). The specific die casting parameters are listed in Table 1. Approximately 100 castings were produced during this experimental run.

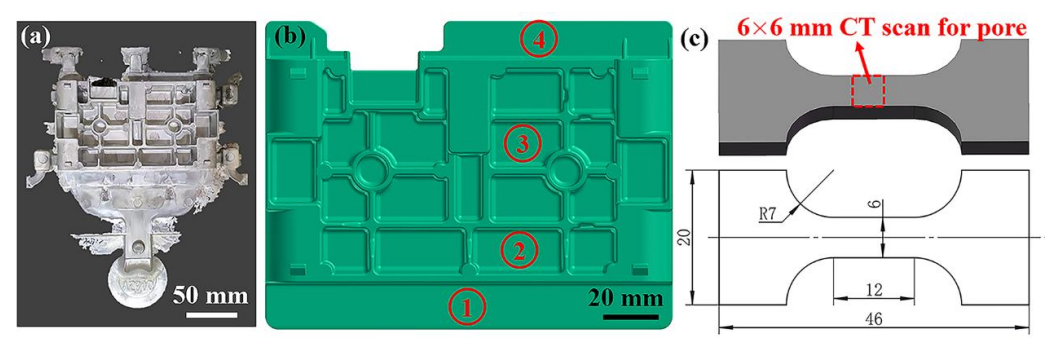


Fig. 1: Casting product, room-temperature tensile sampling locations of the battery module end, and microstructural analysis regions: (a)

Battery module end casting; (b) Locations for tensile specimen extraction; (c) Dimensions of the room-temperature tensile specimens and regions for microstructural analysis

Table 1: The process parameters adopted during HPDC.

Alloy	Slow shot speed	Fast shot speed	Mold temperature	Melting temperature (°C)	Intensification casting
	(m/s)	(m/s)	(°C)		pressure (MPa)
AE81	0.15	6	200	720	30

Tensile specimens at room temperature were sampled from different areas of the battery module end, as shown in Fig. 1(b). The tensile samples featured a dog-bone shape, with detailed dimensions provided in Fig. 1(c), including a gauge length of 12 mm and a width of 6 mm. Additionally, mechanical properties at room temperature were evaluated at various locations of the HPDC AE81 magnesium alloy casting using an electronic universal testing machine (CMT 6305 -300 kN) under a tensile speed of 1 mm/min. Each sampling position was tested three times to ensure reproducibility, and the average value was calculated.

The two-dimensional microstructure of the alloy was examined using a scanning electron microscope (Thermo Scientific Apreo 2S) equipped with a backscattered electron detector (BSE), energy-dispersive spectroscopy (EDS), and electron backscatter diffraction (EBSD) detectors. The observation region corresponded to the red dashed box in Fig. 1(c). For SEM and EBSD analyses, samples were ground stepwise using 600 to 3000 grit abrasive papers and then mechanically polished until a mirror-like, scratch-free surface was Furthermore, EBSD specimens were subjected to electrolytic polishing using an AC2 solution maintained at -30 °C.

A cuboid specimen with dimensions of 6×6 mm was selected from the complete room-temperature tensile

sample for X-ray tomography (see Fig. 1c) to investigate pore distribution. The micro-CT tensile test of HPDC AE81 magnesium alloy was conducted at the Advanced Materials Research Institute, Yangtze Delta. The X-ray microscope (XLAB-2000) operated at 60 kV and 90 μA , providing a spatial resolution of 5.08 μm . After acquiring CT data, the 3D pore morphology was reconstructed using Avizo 2022 software. Relevant morphological parameters such as pore diameter, volume, sphericity, and aspect ratio were extracted from the software.

3 Results and discussion

3.1 Microstructure

EBSD maps of various locations in the battery module end are shown in Fig. 2. It can be observed that several coarse grains are surrounded by numerous finer grains, forming a bimodal-like microstructure. During the HPDC process, once the molten alloy is introduced into the shot sleeve, it first comes into contact with the sleeve wall and solidifies preferentially, forming coarse dendritic or equiaxed crystals. As the fast shot speed stage proceeds, these coarse grains are entrained by the molten flow into the die cavity, resulting in the formation of externally solidified crystals (ESCs). Moreover, several adjacent ESCs in the image exhibit identical crystallographic orientations and distinct high-angle grain boundaries. This implies that these grains possibly derived from a

single ESCs, fragmented by high shear stress during the rapid mold filling. Meanwhile, the fine primary α -Mg grains display diverse orientations and marked anisotropy, suggesting they were formed by rapid nucleation during solidification in the cavity.

Kernel average misorientation (KAM) is commonly used to characterize the density and distribution of geometrically necessary dislocations (GNDs) in alloys, with GNDs density serving as an indicator of internal stress levels. In general, a higher density of GNDs corresponds to greater local strain [31]. Interestingly, numerous low-angle grain boundaries were observed within the coarse grains. KAM maps reveal elevated values near these low-angle grain boundaries, which may be attributed to thermal stresses caused by uneven cooling

rates between the surface and core during solidification. These stresses induce localized plastic deformation and subsequent dislocation accumulation, which explains the increased KAM values. Additionally, during the HPDC high-pressure shear process, may cause plastic deformation of dendrite fragments without fragmentation or dislocation recovery, contributing to high local KAM values in ESCs. Moreover, inverse pole figure (IPF) maps were used to quantify grain sizes at different sampling positions (see Fig. 2e-h), revealing significant variations in average grain size across regions. Specifically, the average grain size in region #1 was clearly larger than in the other three regions, with values of 16.54±3.70 μm, 12.43±3.33 μm, 12.12±3.10 μm, and 11.34±2.45 μm for regions #1 to #4, respectively.

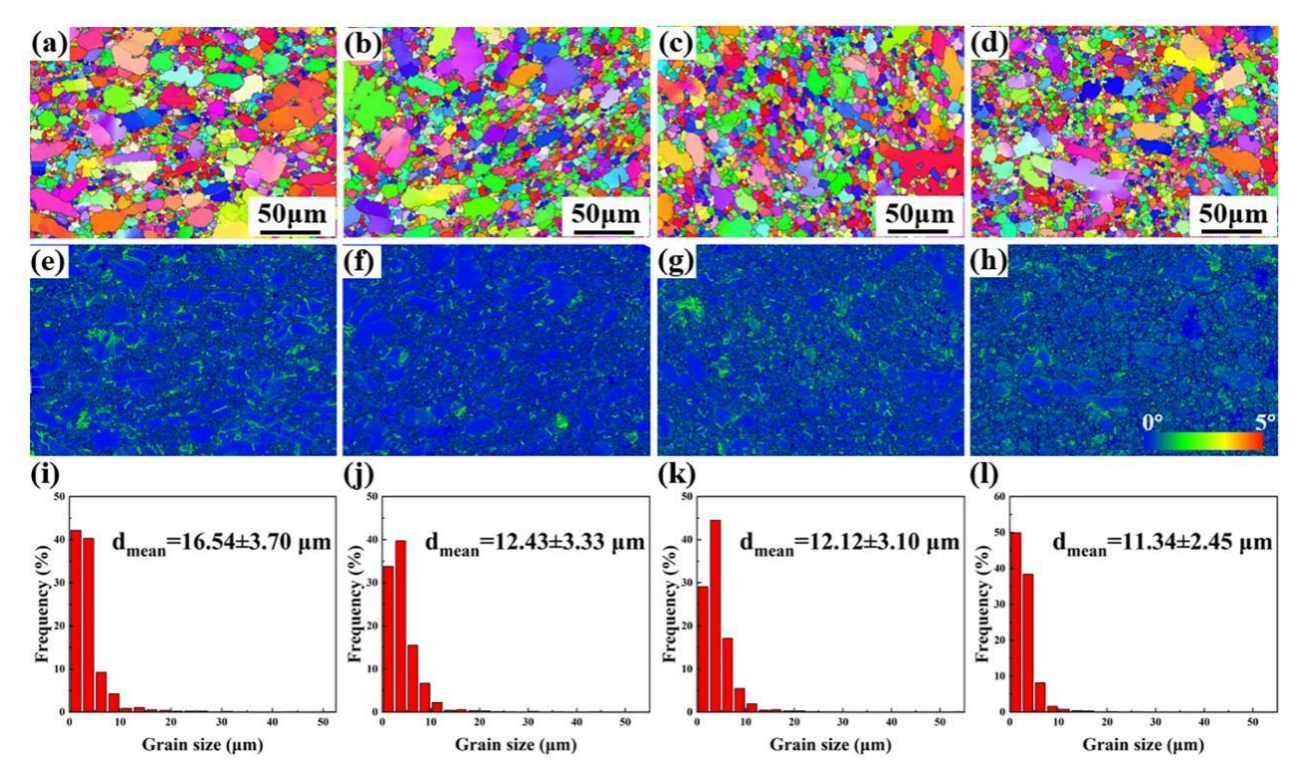


Fig. 2: EBSD microstructures and grain size statistics at different sampling positions: (a)(e)(i) #1, (b)(f)(j) #2, (c)(g)(k) #3, and (d)(h)(l) #4.

Figure 3 illustrates the morphologies of second phases at different sampling positions of the AE81 magnesium alloy battery module end. BSE-SEM analysis reveals that the microstructure primarily comprises an α -Mg equiaxed matrix with multiple intermetallic compounds distributed inside grains and at grain boundaries. Based on morphological features and compositional analysis, four types of second phases are identified: the gray phase commonly found in Mg alloys is Mg₁₇Al₁₂ with a body-centered cubic structure [32]; the

bright white blocky phase is $Al_{10}Ce_2Mn_7$ with a hexagonal crystal system, lattice constants a=0.874 nm and c=1.297 nm $^{[33]}$; the bright white needle-like phase is $Al_{11}Ce_3$, a body-centered orthorhombic structure with space group Imm, and lattice constants a=0.44 nm, b=1.30 nm, c=1.01 nm $^{[32]}$; and the bright white particulate phase is Al_2Ce , which has a face-centered cubic structure with lattice constant a=0.7700 nm $^{[34]}$. Overall, the morphology and distribution of the second phases show little variation across different regions of the AE81 Mg

alloy castings. Moreover, pores were observed in all sampled regions, with detailed characterization of these

pores to be presented subsequently.

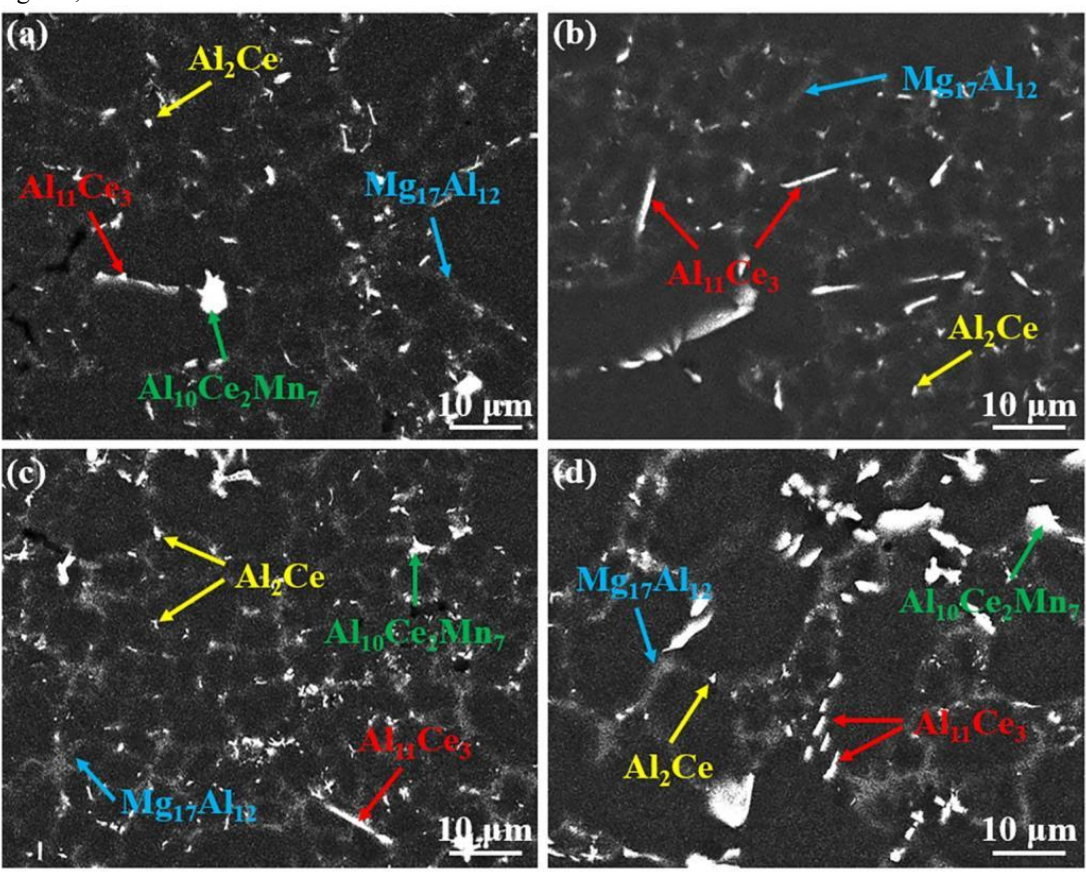


Fig. 3: SEM microstructures at different sampling positions: (a) 1#, (b) 2#, (c) 3#, and (d) 4#.

3.2 Morphology and distribution of pore

Using X-ray CT and image processing with Avizo 2022 software, the 3D morphology and geometric parameters of pores in HPDC AE81 magnesium alloy can be quantitatively characterized. Pores are often described in terms of volume, equivalent diameter, and sphericity; notably, sphericity is crucial as it usually indicates the morphological complexity of the pores. Here, sphericity is defined as the ratio of the surface area of the pore to that of an equivalent sphere with the same volume [35], and can be expressed as:

$$Sph = \frac{\pi^{1/3} (6B_{v})^{2/3}}{S_{v}}$$
 (1)

Here, B_{ν} and S_{ν} represent the volume and surface area of the pore, respectively. When the sphericity approaches 1, the pore is considered a perfect sphere. Based on the pore formation mechanisms and morphology (volume and sphericity) [14, 36-38], pores can be classified accordingly. Earlier research [34] indicates that pore classification

primarily uses two thresholds: a volume of 6.4×10⁴ µm³ (approximately 50 µm diameter) and a sphericity value of 0.5. Classification is determined according to these parameters. Pores are ultimately classified into four types: (1) Net-shrinkage (diameter $> 50 \mu m$, sphericity < 0.5), caused by extensive ESCs aggregation, which obstructs interdendritic liquid feeding and leads to a large, low-sphericity interconnected pore network (Fig. 4c); (2) Gas-shrinkage pore (diameter $> 50 \mu m$, sphericity > 0.5), composed of gas pores combined with surrounding shrinkage pore, also of large size (Fig. 4d); (3) Island-shrinkage (diameter $< 50 \mu m$, sphericity < 0.5), formed due to sparse ESCs aggregation and poor feeding between ESCs dendrites, smaller in size (Fig. 4e); (4) Gas pore (diameter $< 50 \mu m$, sphericity > 0.5), arising from gas entrapment during HPDC, showing spherical shapes under interfacial tension, and further compressed by pressure intensification in the late HPDC process, leading to small, rounded pores (Fig. 4f). This classification is consistent with the findings of Zhang and Yu et al. [37, 38],

第 17 届亚洲铸造会议

revealing from the formation mechanism perspective the synergistic control of ESCs distribution and process parameters on defect morphology.

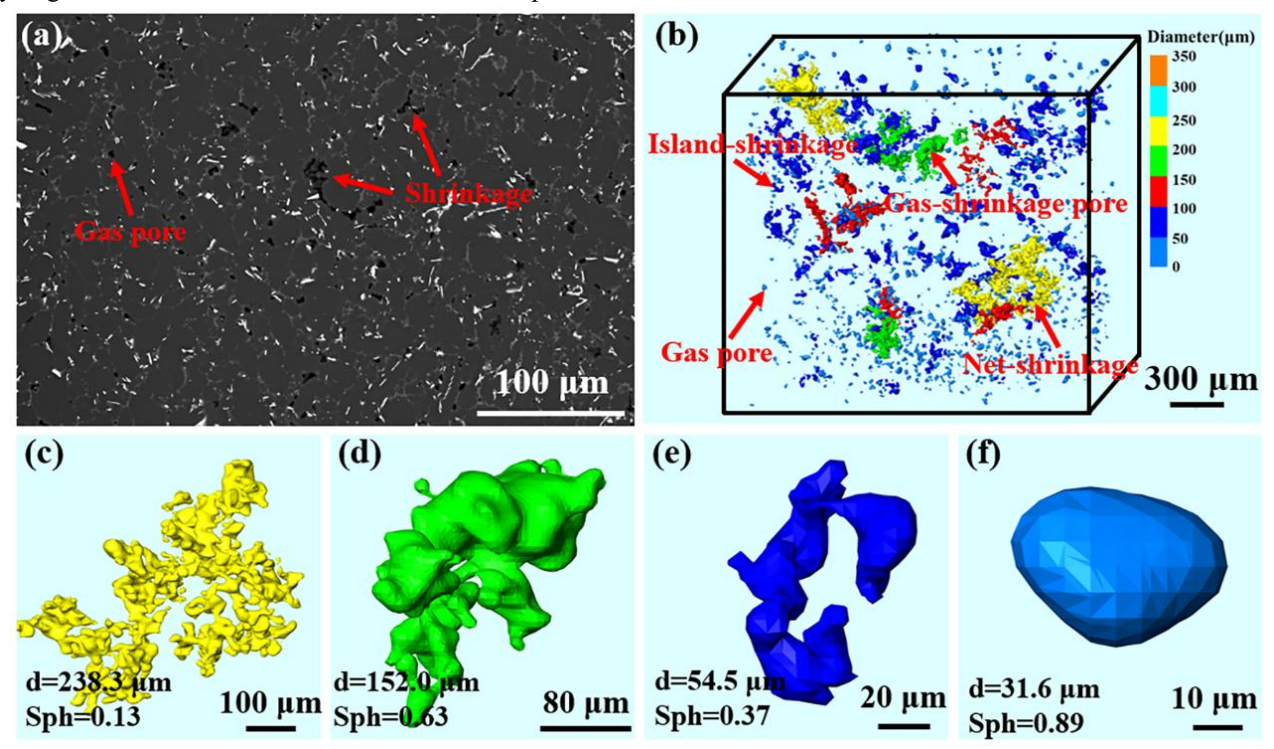


Fig. 4: Typical defects of AE81 magnesium alloy shown by SEM morphology and 3D morphology: (a) SEM microstructure, (b) 3D morphology of pores in HPDC AE81 Mg alloy, (c) net-shrinkage, (d) gas-shrinkage pore, (e) island-shrinkage, (f) gas pore.

Figure 5 illustrates the 3D distribution and morphology of pores in HPDC AE81 magnesium alloy castings at different regions. At position 1#, the pores mainly consist of large-scale interconnected net-shrinkage, gas-shrinkage pores, island-shrinkage, and gas pores. It is evident that this region contains more morphologically complex and larger networked shrinkage pores, with a distinct defect band observable from the XY plane, as shown in Fig. 5(a) and (e). The net-shrinkage at position 2# are significantly reduced compared to position 1#, and the volume and quantity of pores are also markedly smaller, although the pore distribution is uneven, with larger pores concentrated in the lower right corner; The pore morphology at positions 3# and 4# is similar to that at 2#, but the pore distribution is relatively more uniform. Overall, based on the 3D reconstruction results, the number and size of pores at positions 2# to 4# are significantly smaller than those at position 1#.Previous studies have shown that pore morphology and distribution are closely related to

mechanical properties, and a higher density of pore defects may lead to deterioration of mechanical properties [13, 39, 40].

Figure 6 illustrates the distribution of pore sphericity at different sampling locations on the HPDC AE81 magnesium alloy battery endplate. It can be observed that the sphericity values at all four locations are concentrated within the range of 0.1 to 1. Among them, position 1# contains a higher number of pores with sphericity less than 0.5 and diameter greater than 50 µm, indicating a greater presence of net-shrinkage which may severely affect mechanical properties. Positions 2# to 4# show a higher proportion of pores with sphericity greater than 0.5 and diameter also larger than 50 µm, corresponding to more gas shrinkage pores. Gas shrinkage pores generally have much higher sphericity than net-shrinkage, exhibiting more rounded morphologies and potentially causing less stress concentration.

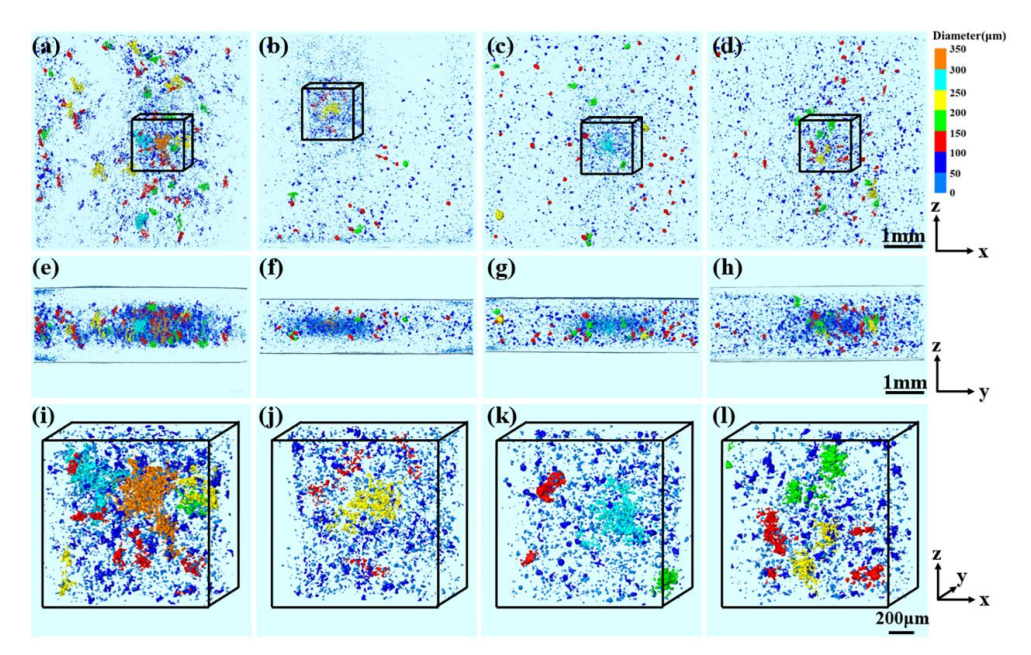


Fig. 5: Pore distribution at different sampling positions of the battery module end: (a)(e)(i) 1#, (b)(f)(j) 2#, (c)(g)(k) 3#, and (d)(h)(l) 4#.

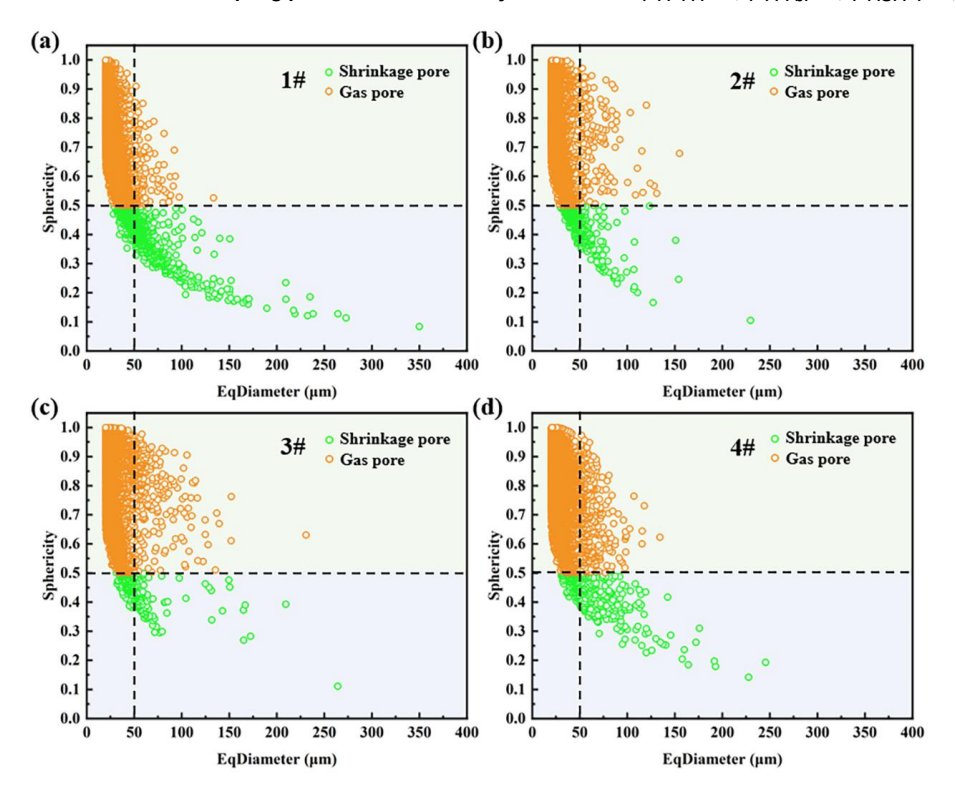


Fig. 6: Statistical analysis of pore sphericity at different sampling positions of the battery module end: (a) 1#, (b) 2#, (c) 3#, and (d) 4#.

3.3 Mechanical properties

increase, which is consistent with the previously observed

Figure 7 illustrates the room temperature mechanical properties of the battery end plate at different sampling locations. The results show that at position 1#, the UTS, YS, and EL at room temperature are 218 MPa, 164 MPa, and 4.3%, respectively. With changes in sampling locations, the YS at positions 2# to 4# are 172 MPa, 175 MPa, and 178 MPa, respectively, showing a slight

increase, which is consistent with the previously observed grain refinement trend. Notably, the UTS at positions 2# to 4# increases by approximately 20 MPa compared to position 1#, and EL improves by about 2-3%. The best room temperature performance is observed at position 4#, with UTS, YS, and EL of 242 MPa, 178 MPa, and 6.8%, respectively. In summary, the battery end plate exhibits excellent room temperature mechanical properties,

meeting the requirements for automotive battery pack

industrial applications.

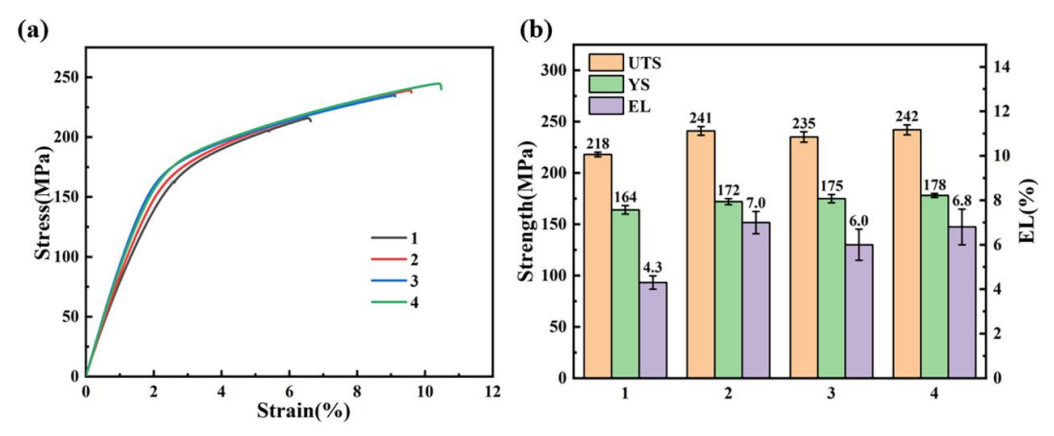


Fig. 7: Room-temperature mechanical properties at different sampling positions of the battery module end.

3.4 Fracture morphology

To further investigate the fracture mechanisms under room-temperature tensile conditions at different sampling positions. The fracture morphologies of different positions were characterized, as shown in Fig. 8. From the locally enlarged images, numerous pores and cleavage planes can be observed at position 1#, suggesting that the fracture mechanism is likely brittle cleavage fracture (Fig. 8a-d). The fracture surface at position 2# shows numerous dimples, tear ridges, and a few cleavage planes, suggesting a mixed ductile-brittle fracture mechanism (Fig. 8e-h). However, at position 3#, more pores and

cleavage facets typical of brittle fracture are observed, along with some tear ridges and dimples on the fracture surface (Fig. 8i-l). Therefore, the fracture mechanism at this position is also likely to be a ductile-brittle mixed mode. At position 4#, a small number of pores and cleavage facets are observed, accompanied by more dimples and tear ridges characteristic of ductile fracture (Fig. 8m-p), resembling the fracture morphology at position 2#, also indicating a ductile-brittle mixed-mode fracture. In summary, the fracture morphology features are consistent with the overall trend of mechanical properties.

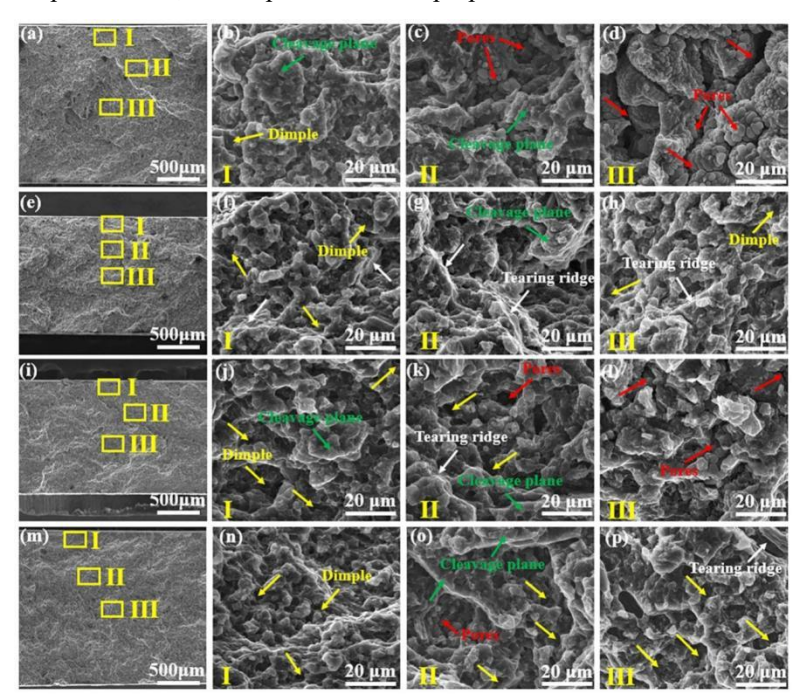


Fig. 8: Fracture surface morphologies at different sampling positions of the battery module end: (a-d) 1#, (e-h) 2#, (i-l) 3#, and (m-p) 4#. 3.5 Influence of casting filling and solidification behavior on microstructure

The microstructure and mechanical properties of the HPDC AE81 magnesium alloy battery module end vary across different locations. The formation of the alloy's microstructure is closely related to the melt filling, solidification behavior, and the structural characteristics of the casting during the HPDC process [19, 20]. To clarify the microstructure formation mechanisms in different regions and their intrinsic relationship with mechanical performance, a systematic analysis of the filling and solidification behavior of the HPDC battery module end was carried out, as shown in Fig. 9. When the filling reaches 34.8%, the melt begins entering the inner gate,

with the overall filling process remaining relatively stable. At 40.4% mold filling, the molten metal flows into the casting cavity, and partially hollow regions appear, indicating possible air entrapment. At a filling level of 53.9%, the melt extends to position 3#, though the bottom areas on both sides remain unfilled. At 70.2% filling, the 4# region is fully filled, but air entrapment may occur at the lower sides of the casting. In summary, the overall filling process of the HPDC magnesium alloy is relatively stable, with air entrapment occurring only in localized areas.

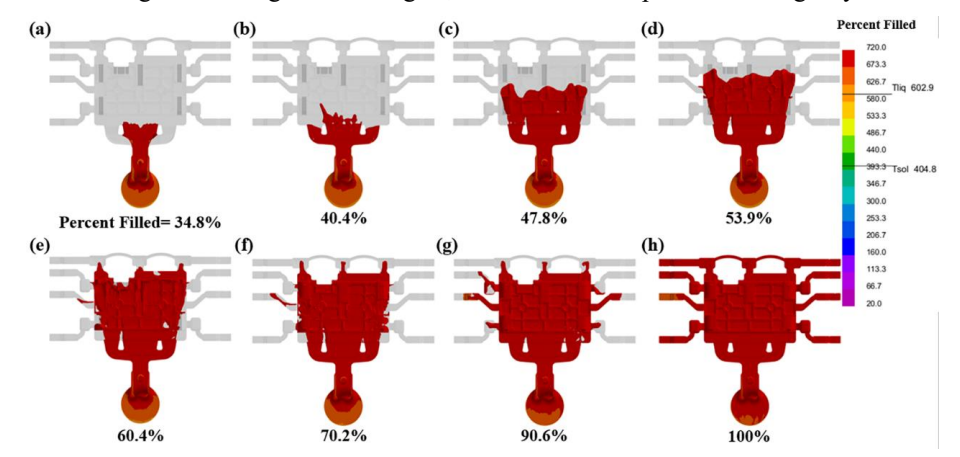


Fig. 9: Simulation results of the mold-filling process of the HPDC AE81 magnesium alloy battery module end component.

In addition, the solidification order was investigated by analyzing the evolution of solid fraction distribution through simulation during the solidification process (see Fig. 10). Simulation results reveal that positions 2# and 3# solidify faster than position 1#. This is due to the 1.5 mm thin-walled structure at positions 2# and 3#, resulting in faster cooling and shorter solidification duration. Consequently, the reduced time for grain growth leads to smaller grain sizes. Hence, the mechanical performance at

positions 2# and 3# is better than that of position 1#. Simulation also shows that the solidification time at position 4# is similar to that at position 1#. However, position 1# is located closer to the biscuit and gate, where the melt temperature is higher, which may result in grain coarsening at this location. Therefore, the finer average grain size at position 4# contributes to its improved mechanical properties compared to position 1#.

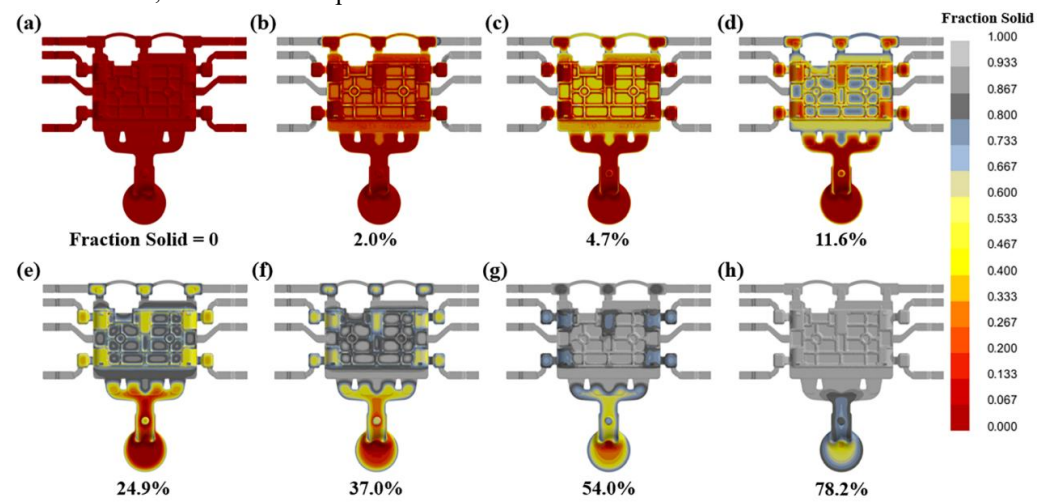


Fig. 10: Simulation results of solid fraction evolution during the solidification of the HPDC AE81 magnesium alloy battery module end component.

第 17 届亚洲铸造会议

3.6 Effect die-casting defects on mechanical properties

The multistage process characteristic of HPDC, including slow shot, fast shot, and intensification pressure, induces heterogeneous nucleation of the melt within the shot chamber, leading to the formation of primary grains and typical ESCs. Additionally, unavoidable air entrapment and insufficient feeding during the HPDC process further result in the formation of pore defects, both of which significantly degrade the room-temperature mechanical properties of the alloy. According to Wang and Zheng [41, ^{42]}, the tensile strength and ductility of HPDC alloys are closely linked to the ESCs' area fraction and size—lower ESCs content usually leads to better mechanical properties. Accordingly, this study measured the ESCs area fraction and average grain size at various positions on the AE81 HPDC battery module end (see Fig. 11). It was observed that the ESCs area fraction at position 1# was 53.09%, whereas it significantly decreased to 34.68% at position 4#. This may be attributed to the high-speed filling process, where the short flow path and complex geometry of the battery module end expose the melt to strong shear forces, resulting in extensive fragmentation of ESCs dendrites and a significant reduction in ESCs area fraction. Similarly, the grain sizes at positions 2# and 3# are smaller than at position 1#, largely influenced by the ESCs content, and also related to the faster solidification rates discussed earlier. Simulation results indicate shorter solidification times at positions 2# and 3#, limiting ESCs growth and resulting in grain refinement. Interestingly, grain size at 4# is larger than at 2# and 3#, possibly because it solidifies more slowly, giving ESCs grains more time to grow and coarsen.

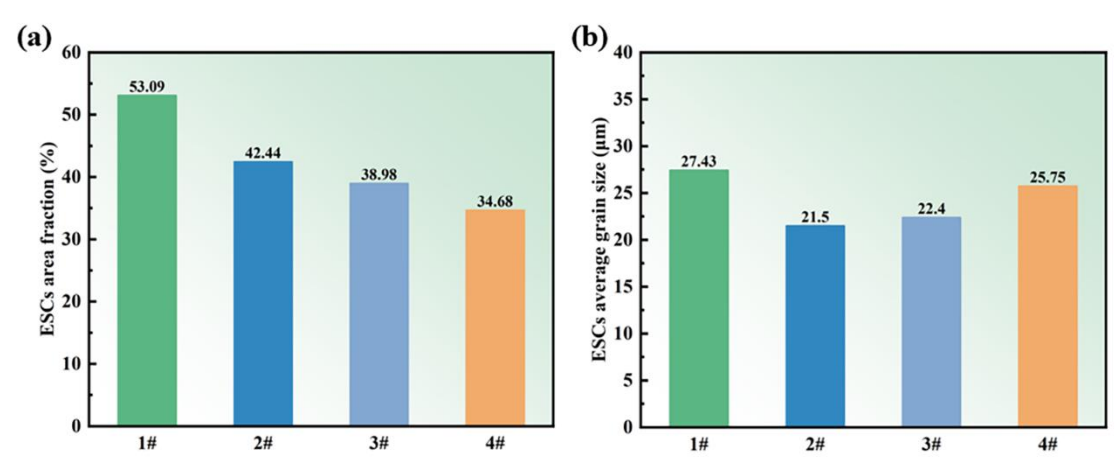


Fig. 11: Statistical results of ESCs area fraction and average grain size at different sampling positions on the battery module end.

Numerous studies have confirmed that pores, as a key microstructural characteristic of HPDC magnesium alloys, exert a decisive influence on their room-temperature mechanical properties [15, 43]. According to our data (see Fig. 12), position 1# has a pore volume fraction of 0.74%, which is about 2.2 times higher than those of positions 2#-4# (0.33%, 0.39%, and 0.34%). This significant porosity variation directly causes a gradient in mechanical performance. The high porosity at position 1# leads to reduced EL and UTS, while the lower porosity at positions 2#-4# results in better mechanical performance. That is, pores act as stress concentration sites, substantially reducing the effective load-bearing area and promoting crack initiation, thereby degrading the mechanical properties. Notably, despite similar porosity among positions 2#-4#, their mechanical behavior differs

slightly, implying that pore size, shape, and distribution pattern also significantly influence performance.

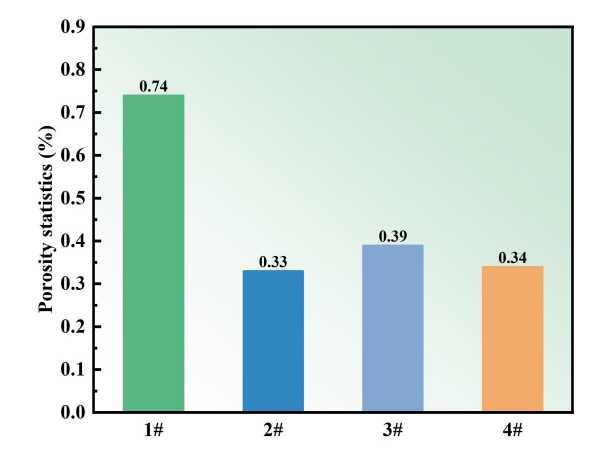


Fig. 12: Quantitative analysis of pore volume fractions at various sampling locations of the battery module end.

Studies have shown that the fracture behavior of HPDC magnesium alloys at room temperature exhibits a significant dependence on pore size, with cracks preferentially initiating at the largest pore defects $^{[14,\,40,\,44]}.$ As shown in Fig. 13, 3D morphological analysis reveals distinct differences in the largest pore characteristics at different locations of the battery module end. The pore in sample 1# exhibits the largest equivalent diameter (349.92 μm) and the lowest sphericity (0.08), whereas the maximum pore parameters for samples 2#, 3#, and 4# are (229.57 μm , 0.18), (264.12 μm , 0.11), and (245.45 μm , 0.19), respectively. These geometric differences lead to

significant variations in mechanical performance: large-sized and low-sphericity pores induce more severe stress concentration, resulting in sample 1# exhibiting the poorest overall mechanical properties. In contrast, the other samples, which possess smaller pore sizes and higher sphericity, demonstrate superior mechanical performance. These findings confirm the critical influence of pore morphological characteristics—particularly equivalent diameter and sphericity—on the mechanical properties of HPDC magnesium alloys.

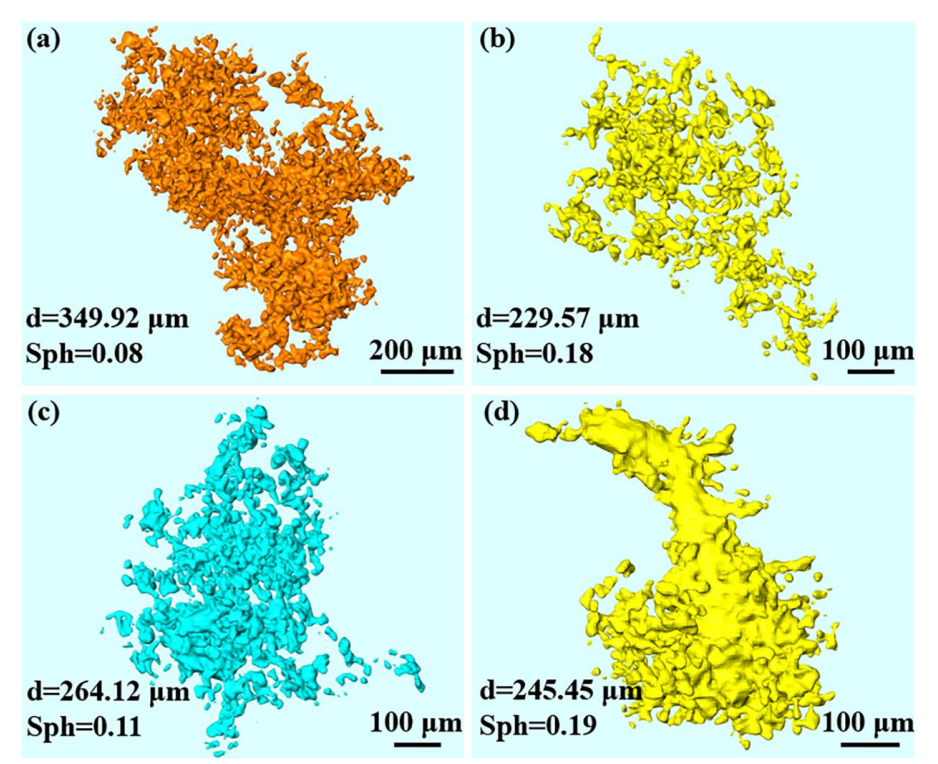


Fig. 13: 3D morphology of the largest pores at different sampling locations on the battery module end: (a) #1, (b) #2, (c) #3, and (d) #4.

4 Conclusion

In this work, thin-walled AE81 magnesium alloy battery module ends were successfully fabricated via HPDC. Combined simulation and experimental studies were conducted to clarify the influence of HPDC filling behavior and solidification sequence on the microstructure and mechanical properties of different regions within the cast components. The main conclusions are as follows:

(1) From the gate to the far end of the casting, the average grain size decreased from 16.54 μ m at position 1# to 11.34 μ m at position 4#. Concurrently, the area fraction of externally solidified crystals reduced from

53.09% to 34.68%, leading to an increase in yield strength from 164 MPa to 178 MPa.

- (2) The elongation and ultimate tensile strength at different sampling positions were significantly influenced by the pore volume fraction. At position 1#, the porosity reached 0.74%, resulting in the lowest elongation (4.3%) and ultimate tensile strength (218 MPa). In contrast, in other regions with reduced porosity (0.33–0.39%), elongation increased to 6–7%, and ultimate tensile strength reached 235–242 MPa.
- (3) The mechanical properties of HPDC AE81 magnesium alloy battery module ends exhibited sampling-location-dependent variation. Yield strength

was primarily governed by the average grain size, whereas elongation and ultimate tensile strength were negatively correlated with pore volume fraction.

Acknowledgement

This work is financially supported by the National Key Research and Development Program of China (grant number 2022YFB3709300, 2021YFB3701000), and the National Natural Science Foundation of China (grant number 52271090, 52071036, U2037601, U21A2048), and Chongqing Science and Technology Commission, China (grant number CSTB2022TIAD-KPX0021), and the Fundamental Research Funds for the Central Universities (grant number SKLMT-ZZKT-2022Z01, SKLMT-ZZKT-2022M12).

Conflict of interest

The authors declare that they have no known competing financial interests or personal relationships that could have appeared to influence the work reported in this paper.

References

- Gjestland H., Westengen H. Advancements in High Pressure Die Casting of Magnesium. Advanced Engineering Materials. 2007, 9(9): 769-776.
- [2] Li Tian, Song Jiangfeng, Zhang Ang, et al. Progress and prospects in Mg-alloy super-sized high pressure die casting for automotive structural components. Journal of Magnesium and Alloys. 2023, 11(11): 4166-4180.
- [3] Xie Hecong, Zhao Hua, Guo Xin, et al. Recent progress on cast magnesium alloy and components. Journal of Materials Science. 2024: 1-34.
- [4] Song Jiangfeng, Chen Jing, Xiong Xiaoming, et al. Research advances of magnesium and magnesium alloys worldwide in 2021. Journal of Magnesium and Alloys. 2022, 10(4): 863-898.
- [5] çam Gürel, Günen Ali. Challenges and opportunities in the production of magnesium parts by directed energy deposition processes. Journal of Magnesium and Alloys. 2024, 12(5): 1663-1686.
- [6] Wang Qinghua, Huang Zhiquan, Zhu Yanchun, et al. Study of Corrosion Behavior of Mg - Gd-Based Soluble Magnesium Alloys. Metals. 2025, 15(1): 35.
- Zhu Yanchun, Wang Niulin, Chu Zhibing, et al. [7] Study of the corrosion mechanism of Mg - Gd

- based soluble magnesium alloys with different initial texture states. Corrosion Reviews. 2023, 41(6): 659-672.
- [8] Zhu Yanchun, Hao Chenrui, Li Ziliang, et al. First-principles study of binary and ternary phases in Mg-Gd-Ni alloys. Physica B: Condensed Matter. 2024, 685: 416065.
- [9] Zhu Yanchun, Wang Qinghua, Huang Zhiquan, et al. Strain hardening exponent and strain rate sensitivity exponent of cast AZ31B magnesium alloy. Metals. 2022, 12(11): 1942.
- [10] Zou Jingfeng, Ma Lifeng, Zhu Yanchun, et al. Gradient microstructure and superior strength ductility synergy of AZ61 magnesium alloy bars processed by radial forging with different deformation temperatures. Journal of Materials Science & Technology. 2024, 170: 65-77.
- [11] Su Chuangye, Li Dejiang, Wang Jie, et al. Enhanced ductility in high-pressure die casting Mg-4Ce-xAl-0.5Mn alloys via modifying second phase. Materials Science and Engineering: A. 2020, 773: 138870.
- [12] Wang Gerry Gang, Weiler J. P. Recent developments in high-pressure die-cast magnesium alloys for automotive and future applications. Journal of Magnesium and Alloys. 2023, 11(1): 78-87.
- [13] Chadha Gurjeev, Allison John E., Jones J. Wayne. The role of microstructure on ductility of die-cast AM50 and AM60 magnesium alloys. Metallurgical and Materials Transactions A. 2007, 38: 286-297.
- [14] Zhang Yongfa, Zheng Jiang, Xia Yatong, et al. Porosity quantification for ductility prediction in high pressure die casting AM60 alloy using 3D X-ray tomography. Materials Science Engineering: A. 2020, 772: 138781.
- [15] Li X., Xiong S. M., Guo Z. Improved mechanical properties in vacuum-assist high-pressure die casting of AZ91D alloy. Journal of Materials Processing Technology. 2016, 231: 1-7.
- [16] Xie Hecong, Wang Jing, Li Yongfeng, et al. Fast shot speed induced microstructure and mechanical property evolution of high pressure die casting Mg-Al-Zn-RE alloys. Journal of Materials Processing Technology. 2024, 331: 118523.
- [17] Qin Xin-Yu, Su Yong, Chen Jian, et al. Finite element analysis for die casting parameters in high-pressure die casting process. China Foundry. 2019, 16(4): 272-276.

- [18] Dou K., Lordan E., Zhang Y. J., et al. A complete computer aided engineering (CAE) modelling and optimization of high pressure die casting (HPDC) process. Journal of Manufacturing Processes. 2020, 60: 435-446.
- [19] Niu Zhichao, Liu Guangyu, Li Tian, et al. Effect of high pressure die casting on the castability, defects and mechanical properties of aluminium alloys in extra-large thin-wall castings. Journal of Materials Processing Technology. 2022, 303: 117525.
- [20] Gunasegaram D. R., Givord M., O'Donnell R. G., et al. Improvements engineered in UTS and elongation of aluminum alloy high pressure die castings through the alteration of runner geometry and plunger velocity. Materials Science and Engineering: A. 2013, 559: 276-286.
- [21] Yang Jian, Liu Bo, Shu Dongwei, et al. Effect of ultra vacuum assisted high pressure die casting on the mechanical properties of Al-Si-Mn-Mg alloy. Journal of Alloys and Compounds. 2025, 1026: 180531.
- [22] Huang Minjie, Jiang Jufu, Wang Ying, et al. Correlation between microstructures and mechanical properties of super-sized new-energy automobile structural component formed by vacuum HPDC process. Journal of Materials Research and Technology. 2025, 36: 1146-1159.
- [23] Qin Ling, Porfyrakis Kyriakos, Tzanakis Iakovos, et al. Multiscale interactions of liquid, bubbles and solid phases in ultrasonic fields revealed by multiphysics modelling and ultrafast X-ray imaging. Ultrasonics Sonochemistry. 2022, 89: 106158.
- [24] Xiang Kang, Qin Ling, Zhao Yuliang, et al. Operando study of the dynamic evolution of multiple Fe-rich intermetallics of an Al recycled alloy in solidification by synchrotron X-ray and machine learning. Acta Materialia. 2024, 279: 120267.
- [25] Qin Ling, Du Wenjia, Cipiccia Silvia, et al. Synchrotron X-ray operando study and multiphysics modelling of the solidification dynamics of intermetallic phases under electromagnetic pulses. Acta Materialia. 2024, 265: 119593.
- [26] Zhang Zhiguo, Khong Jia Chuan, Koe Billy, et al.

 Multiscale characterization of the 3D network
 structure of metal carbides in a Ni superalloy by
 synchrotron X-ray microtomography and

- ptychography. Scripta Materialia. 2021, 193: 71-76.
- [27] Huang Shi, Luo Shifeng, Qin Ling, et al. 3D local atomic structure evolution in a solidifying Al-0.4Sc dilute alloy melt revealed in operando by synchrotron X-ray total scattering and modelling. Scripta Materialia. 2022, 211: 114484.
- [28] Qin Ling, Zhang Zhiguo, Guo Baisong, et al. Determining the Critical Fracture Stress of Al Dendrites near the Melting Point via Synchrotron X-ray Imaging. Acta Metallurgica Sinica (English Letters). 2023, 36(5): 857-864.
- [29] Wang Xueling, Zhao Haidong, Xu Qingyan, et al.

 Tensile damage and fracture of high vacuum die-cast AlSiMgMn alloys with in-situ X-ray microtomography. Materials Science and Engineering: A. 2025, 924: 147869.
- [30] Qin Ling, Maciejewska Barbara M., Subroto Tungky, et al. Ultrafast synchrotron X-ray imaging and multiphysics modelling of liquid phase fatigue exfoliation of graphite under ultrasound. Carbon. 2022, 186: 227-237.
- [31] Hu Chengyang, Zhu Hongyi, Wang Yihao, et al. Microstructure features and mechanical properties of non-heat treated HPDC Al9Si0.6Mn-TiB2 alloys. Journal of Materials Research and Technology. 2023, 27: 2117-2131.
- [32] Zhu S. M., Gibson M. A., Nie J. F., et al. Microstructural analysis of the creep resistance of die-cast Mg - 4Al - 2RE alloy. Scripta Materialia. 2008, 58(6): 477-480.
- [33] Yang Qiang, Lv Shu-Hui, Meng Fan-Zhi, et al. Detailed Structures and Formation Mechanisms of Well-Known Al₁₀ RE₂ Mn₇ Phase in Die-Cast Mg-4Al-4RE-0.3 Mn Alloy. Acta Metallurgica Sinica (English Letters). 2019, 32: 178-186.
- [34] Xie Hecong, Li Yongfeng, Song Jiangfeng, et al. Effect of intensification casting pressure on microstructure and mechanical properties of high pressure die casting AE81 magnesium alloy. Journal of Materials Research and Technology. 2025, 36: 10092-10103.
- [35] Nemcko Michael J., Wilkinson David S. On the damage and fracture of commercially pure magnesium using x-ray microtomography. Materials Science and Engineering: A. 2016, 676: 146-155.
- [36] Li X., Xiong S. M., Guo Z. Correlation between Porosity and Fracture Mechanism in High Pressure

- - Die Casting of AM60B Alloy. Journal of Materials Science & Technology. 2016, 32(1): 54-61.
- [37] Zhang Tong-Tong, Yu Wen-Bo, Ma Chao-Sheng, et al. The effect of different high pressure die casting parameters on 3D microstructure and mechanical properties of AE44 magnesium alloy. Journal of Magnesium and Alloys. 2022.
- [38] Yu Wenbo, Ma Chaosheng, Ma Yihu, et al. Correlation of 3D defect-band morphologies and mechanical properties in high pressure die casting magnesium alloy. Journal of Materials Processing Technology. 2021, 288: 116853.
- [39] Weiler J. P., Wood J. T., Klassen R. J., et al. Relationship between internal porosity and fracture strength of die-cast magnesium AM60B alloy. Materials Science and Engineering: A. 2005, 395(1): 315-322.
- [40] Song Jie, Xiong Shou-Mei, Li Mei, et al. The correlation between microstructure and mechanical properties of high-pressure die-cast AM50 alloy. Journal of Alloys and Compounds. 2009, 477(1): 863-869.

- [41] Wang Qing-Liang, Xiong Shou-Mei. Effect of multi-step slow shot speed on microstructure of vacuum die cast AZ91D magnesium alloy. Transactions of Nonferrous Metals Society of China. 2015, 25(2): 375-380.
- [42] Zheng Huiting, Jiang Yuanhang, Liu Fei, et al. Microstructure heterogeneity optimization HPDC Al-Si-Mg-Cu alloys by modifying the characteristic of externally solidified crystals. Journal of Alloys and Compounds. 2024, 976: 173167.
- [43] Dong Xixi, Zhu Xiangzhen, Ji Shouxun. Effect of super vacuum assisted high pressure die casting on the repeatability of mechanical properties of Al-Si-Mg-Mn die-cast alloys. Journal of Materials Processing Technology. 2019, 266: 105-113.
- [44] Zhang Yongfa, Zheng Jiang, Shen Fuhui, et al. Analysis of local stress/strain fields in an HPDC AM60 plate containing pores with various characteristics. Engineering Failure Analysis. 2021, 127: 105503.